



Development and analysis of a continuous record of global near-surface soil freeze/thaw patterns from AMSR-E and AMSR2 data

5 Tongxi Hu^{1,2}, Tianjie Zhao^{1,3}, Jiancheng Shi^{1,3}, Tianxing Wang^{1,3}, Dabin Ji¹, Ahmad Al Bitar⁴,
Bin Peng^{1,2}, Yurong Cui^{1,2}

¹State Key Laboratory of Remote Sensing Science, Institute of Remote Sensing and Digital Earth, Chinese Academy of Sciences, Beijing 100101, China

²University of Chinese Academy of Sciences, Beijing 100049, China

10 ³Joint Center for Global Change Studies, Beijing 100875, China

⁴Centre D'Etudes Spatiales De La Biosphere, Toulouse, France

Correspondence to: Tianjie Zhao (zhaotj@radi.ac.cn)

Abstract. Monitoring near-surface soil freeze/thaw patterns is becoming essential under the context of global
15 changes as it is more sensitive to climatic fluctuation compared with subsurface thermal characteristics and its
evolution could be an early warning of changes in near-surface permafrost. It requires continuous long term and
stable data record for understanding hydrological, ecological and biogeochemical responses of permafrost to global
climate change. AMSR2 (Advanced Microwave Scanning Radiometer 2) is designed as a successor of AMSR-E
(Advanced Microwave Scanning Radiometer - Earth Observing System) to ensure continuity of such observation.
20 In this study, a linear regression is used to inter-calibrate the AMSR-E and AMSR2 brightness temperatures. Then
discriminant function algorithm is adopted to produce a long term freeze/thaw data record. It is compared with in
situ air temperature measurements from both the temporal and spatial aspects. The results show that the accuracy is
consistent between AMSR-E and AMSR2 with a value above 85%, according to the result of spatial distribution
accuracy. Analysis is conducted with this data record to explore the spatial distribution of frost days, its changing
25 trend and the frost probability of each pixel on a specific date. The mean annual frost days of high northern latitude
(HNL, >45°N) zone is 214.2±69.5 days and the trend of frost days indicates that the frost period is decreasing at a
rate of -0.0065 day/month in 27% of the domain which is defined by significance level of the F-test, and most of
which are concentrated in the high latitude area specifically over the Northeast of Canada, Central and Eastern
Russia and most part of Eastern Europe. The significant changes in frost days mostly occur in regions of
30 discontinuous permafrost and transient permafrost. The spatial distribution of the frost days and its trend variations
are found to be consistent with the minimum temperature anomalies trend. It indicates that the global warming is
not constant at different regions over the globe. Further analysis over the Qinghai-Tibetan Plateau where
discontinuous permafrost, island permafrost, seasonally frozen ground exist demonstrated that the frost period is
shortening slightly over the past decade, and the last frost date is advanced over more than half of the region. It is
35 considered to be a remarkable indication for permafrost degradation in this area.



1 Introduction

Permafrost, defined as subsurface earth materials remaining below 0°C for at least two consecutive years (Dobinski, 2011), occupies approximately 23 million km² or 24% of the exposed land area in the Northern Hemisphere (Zhang et al., 1999). Recently, it has been endorsed by the Global Climate Observing System as one of the essential climate variables and its sensitivity to global warming has recently been emphasised (Harris et al., 2009; Nelson et al., 2001). The near-surface freeze/thaw (F/T) cycle is a unique phenomenon that usually occurs in the upper layer of permafrost that thaws during summer and refreezes completely in winter which is also referred to as the active layer (Schuur et al., 2008). The near-surface freeze/thaw (F/T) cycles and its distribution patterns over landscapes are closely related to changes in permafrost, seasonally frozen ground (Li et al., 2012) and are expected to impact the global water, energy and carbon fluxes (Liou and England, 1998). For instance, the freezing of soil greatly reduces the water infiltration and migration in the soil (Zhang and Armstrong, 2001; Zhang et al., 2003), and in consequence generates a substantial increase in snowmelt runoff (Bayard et al., 2005). Actually, the increasing temperature and melting permafrost not only cause microbial carbon released which in turn warms the climate further (Heimann and Reichstein, 2008), but also unlock an unknown microbial diversity (Frey et al., 2016). Moreover, annual F/T state influences the growing length of the vegetation which is useful to estimate the productivity of forest (Kimball et al., 2001a). Therefore, continuous soil F/T measurement could be used to detect the terrestrial climate signal since it serves as a sensitive indicator of changes at the ground surface.

Measurements of inter-annual variations in the seasonal thawing and refreezing of permafrost soils on regional and global scales are required to understand and refine predictions of the response of permafrost to climate change (Brown et al., 2000). Compared with traditional monitoring conducted through ground-based point measurements, satellite-born microwave remote sensing (McDonald and Kimball, 2005) provides an efficient way to estimate the surface F/T cycles at a relatively large scale. In recent years, several F/T algorithms based on microwave radiation characteristics have been developed including dual-indices algorithm (Zhang et al., 2003; Zuerndorfer and England, 1992), change detection algorithm (Smith et al., 2004), decision tree algorithm (Jin et al., 2009; Jin et al., 2015), and discriminant function algorithm (Zhao et al., 2015). There has been a great interest in L-band technology in recent years due to its large sensitivity to soil water phase transition. The European Space Agency Soil Moisture and Ocean Salinity mission (Kerr et al., 2012) presents the potential to monitor the extent of frozen soil and even frozen depth (Rautiainen et al., 2012; Rautiainen et al., 2014). The Soil Moisture Active Passive (SMAP) mission utilizes the backscatter at L-band to infer the F/T status of soil at a high resolution of 3 km (Entekhabi et al., 2010), but the radar stopped transmitting on July 7, 2015. Despite of these promote technologies, there are also a lot of historical satellite observations including passive radiometers of SMMR (Scanning Multi-channel Microwave Radiometer) (Zuerndorfer and England, 1992), SSM/I (Special Sensor Microwave/Imager) (Judge et al., 1997), and AMSR-E (Zhao et al., 2011) and active scatterometer of QuickScat (Bartsch et al., 2007), ASCAT (Advanced Scatterometer) (Naeimi et al., 2012) and NSCAT (NASA Scatterometer) (Kimball et al., 2001b). Detection of frozen soil with high frequency radiometers is mostly used at the current stage. It relies on its high sensitivity to soil temperature change and a moderate sensitivity to soil water phase transition, with a satisfied accuracy of around 80% (Kim et al., 2011; Zhao et al., 2011). However, the AMSR-E was switched off on 4 October 2011 because of rotation



problems. The AMSR2 took over to continue the observations. China is planning a Water Cycle Observation Mission (Shi et al., 2014; Zhao et al., 2015) to measure the key water cycle elements including the soil F/T with a sensor that has the similar configuration with AMSR-E and AMSR2. It becomes very essential to continue the monitoring of soil F/T with AMSR2 towards a long-term data record. The big challenge is how to obtain consistent measurement of F/T status. Thus, our work was initiated to assess the performances of AMSR-E and AMSR2 brightness temperature data, and remove the observed bias in order to ensure consistency between the two instruments. This inter-calibration methodology based on brightness temperature inter-comparisons has been used for the generation of other consistent and continuous land surface parameter data record, such as soil moisture (Mladenova et al.; Parinussa et al., 2015).

5

10 In this study, inter-calibration of AMSR-E and AMSR2 is first conducted to enable the transfer of original AMSR-E F/T algorithm to AMSR2. A long-term globally F/T data record is then developed based on AMSR-E (2002-2011) and its successor of AMSR2 (2012-present). This continuous F/T data record is validated with *in situ* measurements globally, and the agreement of accuracy between AMSR-E and AMSR2 is assessed and confirmed. With the last more than ten years' (2002-2014) data, the average satellite frost days and its changing trends are calculated and analysed as a preliminary demonstration. In addition, a focus is done on the Qinghai-Tibetan Plateau which has been called the 'third pole' of the Earth. It is a special region of permafrost and seasonal frozen ground in mountain regions in the northern hemisphere. The study of its evolution is conducted through analysis of the duration and extent, the first and last date of frost days.

15

2 Materials and Methods

20 2.1 Passive microwave observations

AMSR-E and its successor AMSR2 share almost the same physical parameters of instruments except slightly difference: AMSR2 has a bigger antenna with the diameter of 2.0 meters while the AMSR-E has a 1.6 meters antenna and a new 7.3GHz channel to eliminate Radio Frequency Interference (RFI) at C-band. Both instruments are operating at an altitude of approximately 700 kilometers orbit that crosses the equator each day at 13:30 local time for ascending orbits and 01:30 for descending. AMSR-E observation has halted because of the antenna problems in November 2011. On 5 December 2012, AMSR-E had been restarted and provided data in Slow Rotation Mode. It can be obtained from the Global Change Observation Mission 1-Water (GCOM-W1) Research Product Distribution Service (Version Release4). This data enables us to inter-calibrate AMSR-E with other radiometers such as AMSR2. The brightness temperatures (T_b , Version 03) we used for AMSR-E are obtained from National Snow and Ice Data Center (NSIDC). For AMSR2, Level 3 standard products (Version 01) are obtained from GCOM-W Data Providing Service. The precipitation product from AMSR-E and AMSR2 (Level 3 standard product) were also used when freeze/thaw status were determined. All the datasets are provided with the Equirectangular projection in the resolution of 0.25 degree globally. AMSR-E slow rotation data are used for inter-calibration with AMSR2. But there is about a 10-month observation gap between the standard products of AMSR-E and AMSR2, which are adopted for the F/T detection.

25

30

35



2.2 Ground based measurements and ancillary data

In general, near-surface F/T cycles responds consistently to forcing by air temperature on an inter-annual basis (Brown et al., 2000). Therefore, daily surface air temperature data from the World Meteorological Organization (WMO) weather stations are used to evaluate and compare the accuracy of F/T data record developed in this study.

5 The temperature data are obtained from the National Climate Data Center (NCDC) as the Global Summary of the Day (GSOD). Previous study has also successfully used these data to evaluate the accuracy of F/T state from SSM/I (Kim et al., 2011). It contains a large number of weather stations distributed widely over the globe, with the maximum temperature (Tmax) and minimum temperature (Tmin) for each day. For the F/T accuracy validation or evaluation in this study, observations of two whole years (2010 and 2013) are selected, as the data in 2010 are used
10 for AMSR-E and the year 2013 is used for AMSR2 after the inter-calibration. It should be noted that any stations with temperature record on a particular day would be used for validation, so the number of validation stations used might vary slightly on a day-to-day basis with a value around 6000.

During the F/T detection, ancillary data were used to improve the accuracy of the classification including the land cover types and precipitation, which has a significant effect on the microwave emission. The MODerate resolution
15 Imaging Spectroradiometer (MODIS) IGBP (International Geosphere-Biosphere Programme) land cover classifications are resampled from a resolution of 0.01 degree to 0.25 degree. The fractional open water coverage (Fw) was calculated based on high resolution grids of 0.01 degree. Grids with Fw >30% are excluded to reduce the influence of open water on microwave emission. The AMSR-E and AMSR2 precipitation products are also used to flag the rainfall areas.

20 To investigate the F/T trend changing we also calculated the global land temperature anomalies trend of the last 14 years (2001-2014) using the gridded mean temperature anomalies dataset namely the Global Historical Climatology Network-Monthly (GHCN-M, Version 3.2.1) temperature dataset. The gridded anomalies were produced by month on a 5° by 5° basis and each month consists of 2592 gridded data points (72 longitude × 36 latitude grid boxes) and also available from 1880 to the most recent month in degree Celsius. The anomalies that is departure from the
25 baseline which is the long-term averages of the latest decade for the 30 years effectively normalizes the temperature and can be compared and combined to more accurately represent temperature patterns with respect to what is normal for different places within a region.

2.3 Methods

2.3.1 Inter-calibration

30 The AMSR-E Slow Rotation Mode data (Level 1 S) and AMSR2 standard data provide us a chance to extract the concurrent observations at almost the same time to adjust the brightness temperature difference introduced by different calibration procedures. In this work, only the land part of Tbs are used as we are focusing on the landscape F/T classification. The period for inter-calibration is designed for one year from 1 August 2013 to 31 July 2014. Only the concurrent observations (±10 minutes between overpass times) at the same grid are matched for
35 comparison. The instrument AMSR2's configurations are coincide with that of AMSR-E so the difference of sensor



characters is assumed to be low. A robust statistical algorithm was used to eliminate the influence of outliers which may occur in the coastlines and regions with large water fraction. This is done by calculating the density of each point at a radius of 0.5 and those data pairs whose density is less than a threshold of 20 are masked out. And then the linear regression model is used to calculate the difference caused mainly by the calibration procedure.

5 2.3.2 Freeze/thaw Discriminant function algorithm

The discriminant function algorithm (Zhao et al., 2011) was originally established with AMSR-E data, aiming to solve the problem of F/T classification under complex surface conditions. It was argued that frozen soil should have a low physical temperature and the water inside soil is partially converted into ice, which indicates the dielectric constant of the soil would decrease. The Tb_{37V} has been found to have a good correlation with the physical
10 temperature and to be insensitive to the water content change (Holmes et al., 2009), so it can be used as a good indicator for distinguishing the frozen soil. In addition, as the water in frozen soil becomes ice, the soil emissivity will increase significantly. It was found that an index called quasi-emissivity can be used to measure the change in soil emissivity. By combining these two criteria, Fisher discrimination analysis was used to establish the discriminant function as follows:

$$15 D_F = 1.47 * Tb_{36.5V} + 91.69 * Qe_{18.7H} - 226.7 \quad (1)$$

$$D_T = 1.55 * Tb_{36.5V} + 86.33 * Qe_{18.7H} - 242.41 \quad (2)$$

$$Qe_{18.7H} = \frac{Tb_{18.7H}}{Tb_{36.5V}} \quad (3)$$

The Qe is called quasi-emissivity. The D_F and D_T represent the discrimination values of frozen and thawed ground, respectively. When $D_F > D_T$ the surface is classified as frozen, otherwise, it is classified as thawed. The discriminant
20 function algorithm has been previously assessed using MODIS land surface temperature and *in situ* soil temperature, and was found to have excellent accuracy in the area of China (Chai et al., 2014). Thus, it is selected to be used in our study.

2.3.3 Comparison with external data

The F/T state data derived from the discriminant function algorithm (using both AMSR-E and AMSR2 data) are
25 compared with the *in situ* air temperature derived from GSOD as the reference dataset. It is assumed that the satellite overpass time (13:30 and 01:30) are corresponding to the level of daily maximum and minimum temperature respectively, although the air temperature generally varies from day to night. The F/T classification based on air temperature should rely on the threshold. In this comparison we use a cut off of 0 °C, which is consistent with other studies (Kim et al., 2011; Zwieback et al., 2015). And when more than one station is located in single grid cell of
30 the satellite data, the average temperature of these stations is used to define the F/T state. The agreement between the two F/T classification is expressed by the accuracy (defined as Acc) in terms of percentage (%), which is the ratio between the correct classifications and the total number of instances. It is calculated as:

$$Acc = \frac{FF+TT}{FF+FT+TF+TT} * 100\% \quad (4)$$



Where the FF is the correct classification number when the soil is frozen and detected as frozen. FT is the incorrect classification number when the soil is frozen but detected as thawed. TT and TF are similar as above.

3 Results

3.1 Inter-calibration between AMSR-E and AMSR2

5 The inter-calibration is conducted for all frequencies available with ASMSR-E and AMSR2 at a global scale (only observations over land are used here). Only results of frequencies used in the F/T classification are presented as in Fig. 1. The data points are filtered by using the pre-defined statistical threshold to exclude some outliers. This is done to focus on the main difference of the majority observations. The inter-calibration coefficients (including the slope and intercept) were derived by linear regression and the coefficients of determination (R-square) are as high
10 as 0.98, which indicates the observations from AMSR-E and AMSR2 are quite close and the transfer of F/T algorithm from AMSR-E to AMSR2 is feasible. But, the RMSD values of the two sensors' observation range from 3 K to 5.5 K, which is not acceptable to elaborate a continuous data record of F/T classification. This difference is associated to physical system configurations or to the calibration procedures which should be taken into account when the same algorithms are applied to both instruments. It is confirmed that there is a consistent warm bias of
15 about 0 K to 3 K with AMSR2 compared with AMSR-E, which is consistent with a preliminary research by Japan Aerospace Exploration Agency (JAXA) (Okuyama and Imaoka, 2015). These differences are then removed by applying regression models to the AMSR2 data. It should be noted these results might change if JAXA made any recalibrations to AMSR2 (Version 01 is used in this study). The correction models used are as follows:

$$Tb_{AMSR_E_18.7h} = 1.0189 \times Tb_{AMSR2_18.7h} - 5.2717 \quad (5)$$

20 $Tb_{AMSR_E_18.7v} = 1.0577 \times Tb_{AMSR2_18.7v} - 16.2042 \quad (6)$

$$Tb_{AMSR_E_36.5h} = 1.0073 \times Tb_{AMSR2_36.5h} - 4.7723 \quad (7)$$

$$Tb_{AMSR_E_36.5v} = 1.0135 \times Tb_{AMSR2_36.5v} - 6.3914 \quad (8)$$

$Tb_{AMSR_E_18.7h}$ is the 18.7GHz horizontal-polarization brightness temperature observed by AMSR-E. These models are adopted to construct a consistent long-term brightness temperature observed by these two sensors.

25 3.2 Accuracy of the freeze-thaw data record and its consistency assessment

A long term F/T data record is obtained by the discriminant function algorithm with the AMSR-E and bias-corrected AMSR2 data. Areas with precipitation are masked out based on the Level 3 physical parameters products of AMSR-E or AMSR2. The total accuracy of this derived data record along with its four components (FF, FT, TT, TF) are evaluated for the year of 2010 and 2013, which correspond to the AMSR-E and AMSR2, respectively. Results (Fig.
30 2) show that the discriminant function algorithm developed F/T data record has an overall accuracy of 90.46% and 85.49% respectively for the ascending (A) and descending orbits (D) when compared with the NCDC weather station temperature. This is better or comparable with previous studies (Kim et al., 2011). The small differences in



accuracy of ascending and descending may have many contributing causes, and one of these is the hypothesis that the satellite overpassing time is near to the moment when the highest or lowest temperature occurs during a day. The pattern of seasonal variation of these accuracies is quite similar for the year of 2010 and 2013. The accuracy can reach to 96.58% (A) and 92.09% (D) from May to October when most soils are thawed, and falls to 86.17% (A) and 85.21% (D) from November to January for the Northern Hemisphere. However, the accuracy varies from 70.62% to 97.0% during the spring and autumn seasons, which is expected as the freeze-thaw processes happen frequently and repeatedly that mixed pixels are more likely to be presented. The incorrect classifications (FT and TF) are generally at a low level over the whole year, while the correct classifications (FF and TT) are varying a lot depending on the temperature. Especially for ascending orbits, the incorrect classifications mostly appear to be the case of TF.

5

10 It is reasonable the *in situ* measured air temperature could rise above 0 °C while the ground soil is still frozen during the daytime.

In addition to the temporal variation, the average accuracy for each station for a particular year is calculated to demonstrate the spatial distribution of accuracy as shown in Fig. 3 and Fig.4. Generally, the accuracy is found to vary with latitude and elevation (average 78.05% when latitude >45°N, while 93.54% when latitude between 0°N and 45°N), and generally decreases as the latitude or altitude increase (more freezing/thawing events occur). This indicates that for the high latitude zone and high elevation zone the near-surface soil freeze/thaw cycles are more frequent and complex due to the spatial heterogeneity within passive microwave observations. Moreover, the areas close to water have a relatively low accuracy (about 60%) such as Japan, the Great Lakes and coastlines (Fig.3), although a water fraction flag is used in the algorithm. To investigate the influence, we further analysed the relationship between water fraction and the classification accuracy (Fig. 5), the result indicated that the more the water in a pixel, the lower the accuracy becomes. It may come from that water has influence on the quasi-emissivity so that the discriminant algorithm can't work effectively. These results indicate that the monitoring of freeze/thaw status requires high resolution of observations (such as Sentinel-1 from ESA as SMAP radar is off) and the validation measurement on the ground needs to be match with the satellites.

15

20

The spatial patterns of accuracy (Fig. 3 and Fig. 4) from AMSR-E and AMSR2 are generally consistent, indicating the transfer of the algorithm from AMSR-E to AMSR2 might be successful. To further investigate the consistency of this data record, the classification accuracy for different years/sensors is compared at a station-to-station basis. Without a major climatic difference, the accuracy of the same place from different years or sensors should be at the same level. As shown in Fig. 6, each cross represents one station with X-axis accuracy of AMSR-E and Y-axis of AMSR2. The slope is 0.857 with a small offset of 0.143 and the correlation coefficient between the two years/sensors accuracy is as high as 0.808. To further confirm its consistency, the histograms of accuracy was analysed (Fig. 7) and it also shows a similar frequency distribution. The small offset between these two may be contributed to the climatic variation. This indicates that the consistency of the F/T data record developed from AMSR-E and AMSR2 sensors is confident after inter-calibration.

25

30



3.3 Frost days

With the confidence of the discriminant function algorithm and inter-calibrated observation data, the daily F/T state during the last ten years was developed (2002-2011, 2012-2014, more than 10 years for now). It should be noted that there exists a gap from 2011 to 2012 because of no complete observation for these two years for both AMSR-E and AMSR2, and we are assuming that this gap doesn't make much significance to the long-term analysis of the last ten years. A frost day is a period of 24 hours in which the minimum temperature is equal to or below 0 °C. The frost day and its first and last dates have great impacts to the agriculture, construction and transportation industry. Traditionally, the information of frost is obtained from weather station data. With satellite observation, especially F/T status identified by AMSR-E/AMSR2 sensor, the frost day could be captured by assuming the descending time is approximately the time when the minimum temperature occurs. With the long-term F/T data record developed in this study, we are able to calculate the satellite frost days, trends in frost day at a global scale and also the frost probability of a special day.

The frost days from satellite of a year are defined as below:

$$\text{frost days} = \sum \text{days frozen at descending time} \quad (9)$$

A climatology of frost days during the past decade (Fig. 8) was calculated at a global scale. The mean annual frost days of high northern latitude (HNL, >45°N) zone is 214.2±69.5 [spatial standard deviation] days which coincides with the result of a non-frozen of the high northern latitude period of 177.6±47.6 days by (Kim et al., 2012). And over the low latitude (<45°N) zone of the northern hemisphere, the frost days changes with the seasonal alternation and most frost occurs mainly from late fall to early spring except some mountainous regions. The frost days generally increase as the latitude increases except some special mountain regions such as the Tibet Plateau. The average frost days soar up to 109.48 days with a large standard deviation of 96.54 days in the latitude of 35-40°N compared to the zone in the latitude of 25-30°N which is 19.03±52.63 days. The frost days from satellite could serve as an important reference dataset for other parameter retrievals (Zwieback et al., 2015). For the Southern Hemisphere, frost occurs mainly on the Andes Mountains.

3.4 Anomalies trend analysis of frost days

The long-term dataset also provides an opportunity to analyse the temporal trends of the frost days. Temporal trends are obtained based on the linear least-square regressions with a statistical significance of 90% confidence level (F-test) for each pixel. Only those pixels satisfying the F-test (with significance p value less than 0.1) are accepted for further analysis, and those pixels with p value more than 0.1 are considered as no trend. Results are shown in Fig. 9. The global trends map indicates that the frost days are decreasing in 27% of the domain (defined by the F-test level, p<0.1), and 92.96% of the decreasing region is located at the North Hemisphere at a rate of -0.0065±0.01 days/month, which indicates a substantial warming for North Hemisphere region, especially over the Northeast of Canada and Russia and most part of the Europe region. On the other hand, a cooling trend is found that takes about 38.8% of the whole domain which also mainly occurs in the North Hemisphere with a fraction of 91.67% at a rate of 0.007±0.01 days/month. The cooling region is mainly distributed in the central and eastern US and some other



regions over Asia including the Northeast of China. Besides, there are 34.2% of the domain are considered as no significant trend that does not meet the requirement of F-test criteria. This may provide us a new tool to examine the potential climate changes and regional responses of hydrological and carbon cycle which is highly related to the freeze/thaw processes.

5 3.5 Frost Probabilities

The probability of frost on a special day is obtained by dividing the total number of frost days by the total number of days with satellite observation during the study period. Fig. 10 shows the distribution of frost probability on 1 Jan. and the subgraph demonstrate the frost probability varying with time at a single pixel. The frost probability also depends on the latitude and seasons. The subgraph is only an example and it will change when the location varies. The location in the graph (where the green square locates) is of large probability (almost 1) to freeze from about the day of 1 to 90 days and after 300 days which corresponds to the spring and winter season of the northern hemisphere. The probability increases as the day of year grows at the turn of fall to winter and decreases gradually from spring to summer. This probability map may provide very useful information for land surface or hydrological model. It can also serve as a detailed ancillary dataset for the retrieval of soil moisture as the soil moisture when it freezes does not have clear physical meaning and should be excluded.

3.6 Evolution in the Qinghai-Tibetan Plateau

3.6.1 Spatial and temporal distribution of frost days

The Qinghai-Tibetan Plateau is one of the most sensitive regions to recent climate fluctuations with a general trend of warming. Therefore, we make a further focus on this mountainous region. To explore the spatial and temporal distribution features of the frost days in the Qinghai-Tibetan Plateau, average frost days and their standard deviation from August to October and from March to May were calculated based on the F/T data record. In Fig. 11a, average frost days in end of fall time is 58.4 ± 7.23 days and 55.78% of this area has a length of more than 60 days, only about 22.54% is less than 30 days. The frost day decreases from west to east following the topographic changes. While the frost day standard deviation (Fig. 11b) has a reverse trend, it increases from west to east. The pixels with frost more than 60 days have a standard deviation of 6.04 days while that with frost period less than 30 days has a deviation of 6.96 days. Similarly, the average frost days during March to May is 79.16 ± 3.85 . Pixels with frost days more than 60 take 85.78% of the domain with a low standard deviation of 2.98 days. Pixels with frost days less than 30 only take 5% of the domain and the standard deviation is greater than 5.87 days (Fig.12a and Fig.12b). Because of the topography effects, the frost days in the west of Plateau are longer and stable while in the east the frost days are shorter and has much wide dynamics.

The Fig.13 further shows the daily frost area fraction of the Plateau. Generally, the maximum area fraction does not change much during the past ten years. The peak appears in the winter of each year and can reach to 95% of the whole areas, while the minimum value has more variation. In summer (from July to September) of 2005, 2006 and 2010, the minimum area fraction is as low as 20% and the frost days also drop to about 11 days. This may be associated to climatic anomalies in these summers.



3.6.2 Frost period and its anomalies trend

Here we present a statistical analysis of the frost period in this high elevation mountainous region. Average number of frost days of each month and of all pixels was calculated from October 2002 to December 2014 as shown in Fig. 14. The gap from October 2011 to July 2012 is skipped because of lack of observation. The frost period is about 5 10-15 days from July to September during which the temperature reaches the maximum of a year, while it can reach to 30 days in December and January. In Fig.15 the anomalies trend of the frost period is presented with the standard deviation in light blue. Although the time range is limited, it is found a week declining trend in the last ten years with a value of 0.0013 day.

3.6.3 First and last frost occurrences

10 First and last dates of frost are important to the global vegetation growth. Usually in the North Hemisphere, the first frost happens in the period from late fall to early winter while the last date occurs in the period from late spring to early summer. Therefore, we identify the first frost day of a pixel when it was classified as frozen from 1st July and the successive two days are also classified as frozen for avoiding the influence of abnormal frost. Fig 16a shows the average first date of frost in the Qinghai-Tibetan Plateau in the last ten years. 57.16% and 12.03% of the area begins to freeze in July and August and most of them are distributed in the west of the plateau. The first frost that happens 15 in September and October takes about 26.63% of the area and most are located in the central and east of the plateau. Only about 0.031% begins to freeze after November which are in the southeast of the area. To investigate the changing trend of the first frost dates during the last ten years, the regression analysis prediction method is applied to each pixel. As displayed in Fig 16b, 33.83% of the area keeps stable (here we assume pixels with trend value 20 between -0.01 and 0.01 are stable). 26.2% has a postponed trend with an average value of 0.663 ± 0.78 days/year, and 38.23% has an advanced trend with an average value of -0.549 ± 0.793 days/year under F-test significance (p-value < 0.01).

The last date of frost is identified when the first three successive thawing days appears before 1st July. If a pixel was classified as thawed two days or less before 1st July, then the last date of this grid is considered as 1st July. Fig.17a 25 shows the distribution of the average last date of frost. In the first three months, no more than 10% of the area begins to thaw. In April, about 16.15% begins to thaw, and then expands very quickly during May and June which take about 71.56% of the area. There is no significant changing trend for 27.8% of the area (Fig.17b). About 53.23% has a trend of advance, while 27.8% presents a postponed trend. It indicates more areas in the Qinghai Tibetan Plateau are becoming thawed earlier. The postponed and advanced trend of first and last frost should have a close connection 30 with the temperature change during the last ten years that will be discussed later.

4 Discussion and conclusion

The evolution of permafrost and frozen grounds is becoming essential under the context of global changes. Remote sensing technique could play an important role in unveiling the processes from the monitoring of variables related to the permafrost state, such as the near-surface F/T cycles. In addition, for most practical applications in ecology



or engineering, the immediate reaction of near-surface layers of permafrost and seasonally frozen ground is of primary importance (Anisimov et al., 1997) because most exchanges of energy, water, and carbon between the atmospheric and terrestrial systems occur through it (Nelson et al., 2001). A continuous long term and stable data record is required for understanding the hydrological and biological responses of freeze/thaw to the warming climate.

5 In this study, the observations from AMSR-E and its successor AMSR2 are inter-calibrated to support a long-term data record development of F/T pattern over the global land surface. The F/T state data record is produced by using the discriminant function algorithm with ancillary information of land cover and precipitation. It is validated with an external temperature data from the NCDC with numerous in situ measurements. The result shows that even though these two sensors share almost the same configuration they do have a little difference (3-5.5K) in the

10 observation because of different calibration progress and other issues. This difference should be modified when the two observation date are used with the same algorithm to produce a long-term data product.

The AMSR-E algorithm used in this study was validated using in situ 4-cm soil temperature with a high accuracy of 86% in China (Zhao et al., 2011). The accuracy of the new developed F/T data record is further compared with in situ air temperature measurements at a global scale. It is found the results has a high confidence with overall

15 classification accuracy of 90.46% and 85.49% for ascending and descending orbits, respectively. The accuracy for ascending time is better than descending time. One of the reasons may be associated to that the Tmax air temperature is much closer to soil temperature at 13:30 than Tmin air temperature to soil temperature at 1:30. It is also found that the spatial heterogeneity is an important factor influencing the classification accuracy, as the accuracy could become lower when the temperature is close to the point of soil freezing and thawing. A special case of surface

20 heterogeneity is the influence on the accuracy of the water fraction. It is found the accuracy decreases gradually as the water fraction increases. The accuracy also can be low over mountainous areas because of high topography effects of microwave observations. A potential way to reduce heterogeneity effects may be high resolution observations from active microwave remote sensing like radar or scatterometer. It should be noted that the precipitation also has an impact on the F/T classification results. There are still some artefacts although a

25 precipitation mask is used during the production process. Generally, the accuracy from AMSR-E and AMSR2 is found to be consistent with a correlation coefficient of 0.808 between the two sensors. This is an essential confirmation for the long term study and trend analysis in this study.

Frost probability, frost days and its changing trend is analysed for the first time at a global scale from satellite observation. The climatology of frost days during the past decade show that the mean annual frost days of high

30 northern latitude is 214.2 ± 69.5 days. The frost days decrease in 27% of the domain, specifically over the Northeast of Canada, Central and Eastern Russia and most part of Eastern Europe. And an increasing trend is found that takes about 38.8% of the domain in the Central and Eastern US and the Northeast of China. The spatial distribution of the frost days and its trend varies is considered to be related to the temperature anomalies, indicating that the global warming is not constant at different regions over the globe. We further compared it with the last 14 years' (2001-

35 2014) minimum temperature anomalies trend as shown in Fig. 18. The changing trends are generally consistent with the frost days except some differences in few regions. 49.73% of the domain has an increasing trend while 44.85% has a decreasing trend. These pixels which have an evident trend are mainly located in the Northern Hemisphere.



About 51.02% of the North Hemisphere has an increasing temperature at a rate of 0.00395 °C/month while 47.96% are cooling down at a rate of -0.00529 °C/month. Similarly, as the frost day, the warming areas are mainly in Eastern Europe, North-eastern Canada and Russia, and the cooling areas are mainly in Central and Northeast of US, Central Asia and Northeast of China.

5 For the mountainous area of the Qinghai-Tibetan Plateau, 55.78% of this area has a length of more than 60 days being frost from August to October with a low standard deviation of 2.98 days, while those areas with frost days less than 30 days have a higher standard deviation of 5.87 days. The frost period in the west and center of Plateau, where continuous, island permafrost is distributed, lasts longer and remains stable. In the east the frost days are shorter and has considerable dynamics, where middle-thick seasonally frozen ground are distributed. It indicates
10 the frost days as well as the first and last occurrence of frost changes are closely related to the type of permafrost or seasonally frozen ground. Moreover, the permafrost in Qinghai-Tibetan Plateau has more ice so it is sensitive to climate change (Cheng and Wu, 2007). The frost period is found to present a weak shortening trend, and the last frost date is advanced over more than half of the region, such as the Qaidam Basin. This is the sign of permafrost degradation which would have global implications since permafrost thawing is enhancing the release of greenhouse
15 gases, and therefore serve as a positive feedback to the Earth's climate.

Remote sensing of permafrost is challenging, as microwave sensors are capable of sensing F/T processes only at the upper layer of soil. The physical subsurface characteristics (ground temperature, ice content and thaw depth) are not directly measurable with penetration capabilities of most remote sensing systems. However, there is a large diversity of properties for remote sensing from which the permafrost state can be indirectly derived, including the
20 thermokarst features, seasonal transition of F/T cycles and the phase transition water content (Zhang et al., 2010), which are important features of permafrost dynamics. The results presented in this paper indicates that the instability and trend of permafrost, seasonally frozen ground might be detected based on a change in the near-surface soil F/T cycles. Furthermore, the F/T state of the near-surface is directly or indirectly related to thermal subsurface conditions in conjunction with thermal modelling. By exploiting the advantage of spatial information of this remote sensing
25 data record at regional and global scale, the best possible estimate of thermal state of active layer could be achieved.

5 Acknowledgments

This study was jointly supported by the National Key Basic Research Program of China (2015CB953701), the Strategic Priority Research Program for Space Sciences (XDA04061200) of the Chinese Academy of Sciences, and the National Natural Science Foundation of China (41030534, 41301396). The station-based air temperature data
30 are archived at the NOAA National Climatic Data Center. The global land temperature anomalies is available on the NOAA GHCN Gridded Products website. Research product (AMSR-E LIS) is provided by the GCOM-W Research Product Distribution Service, Japan Aerospace Exploration Agency (JAXA). AMSR2 data was provided by the GCOM-W Data Providing service, JAXA.



References

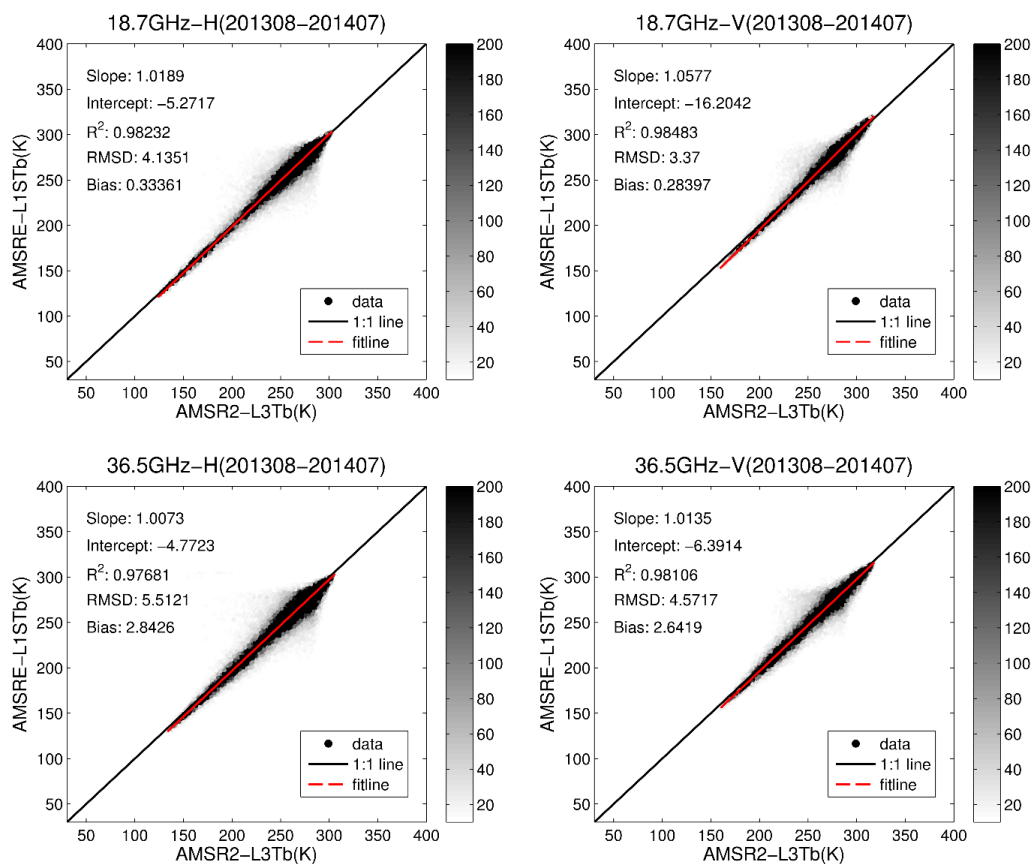
- Anisimov, O. A., Shiklomanov, N. I., and Nelson, F. E.: Global warming and active-layer thickness: results from transient general circulation models, *Global and Planetary Change*, 15, 61-77, 1997.
- Bartsch, A., Kidd, R. A., Wagner, W., and Bartalis, Z.: Temporal and spatial variability of the beginning and end of daily spring freeze/thaw cycles derived from scatterometer data, *Remote Sensing of Environment*, 106, 360-374, 2007.
- Bayard, D., Stähli, M., Parriaux, A., and Flüher, H.: The influence of seasonally frozen soil on the snowmelt runoff at two Alpine sites in southern Switzerland, *Journal of Hydrology*, 309, 66-84, 2005.
- Brown, J., Hinkel, K., and Nelson, F.: The circumpolar active layer monitoring (calm) program: Research designs and initial results 1, *Polar geography*, 24, 166-258, 2000.
- Chai, L. N., Zhang, L. X., Zhang, Y. Y., Hao, Z. G., Jiang, L. M., and Zhao, S. J.: Comparison of the classification accuracy of three soil freeze-thaw discrimination algorithms in China using SSMIS and AMSR-E passive microwave imagery, *International Journal of Remote Sensing*, 35, 7631-7649, 2014.
- Cheng, G. and Wu, T.: Responses of permafrost to climate change and their environmental significance, Qinghai - Tibet Plateau, *Journal of Geophysical Research: Earth Surface*, 112, 2007.
- Dobinski, W.: Permafrost, *Earth-Science Reviews*, 108, 158-169, 2011.
- Entekhabi, D., Njoku, E. G., O'Neill, P. E., Kellogg, K. H., Crow, W. T., Edelstein, W. N., Entin, J. K., Goodman, S. D., Jackson, T. J., and Johnson, J.: The soil moisture active passive (SMAP) mission, *Proc. IEEE*, 98, 704-716, 2010.
- Frey, B., Rime, T., Phillips, M., Stierli, B., Hajdas, I., Widmer, F., and Hartmann, M.: Microbial diversity in European alpine permafrost and active layers, *FEMS microbiology ecology*, 92, fiw018, 2016.
- Harris, C., Arenson, L. U., Christiansen, H. H., Eitzelmüller, B., Frauenfelder, R., Gruber, S., Haeberli, W., Hauck, C., Hölzle, M., and Humlum, O.: Permafrost and climate in Europe: Monitoring and modelling thermal, geomorphological and geotechnical responses, *Earth-Science Reviews*, 92, 117-171, 2009.
- Heimann, M. and Reichstein, M.: Terrestrial ecosystem carbon dynamics and climate feedbacks, *Nature*, 451, 289-292, 2008.
- Holmes, T., De Jeu, R., Owe, M., and Dolman, A.: Land surface temperature from Ka band (37 GHz) passive microwave observations, *Journal of Geophysical Research: Atmospheres (1984–2012)*, 114, 2009.
- Jin, R., Li, X., and Che, T.: A decision tree algorithm for surface soil freeze/thaw classification over China using SSM/I brightness temperature, *Remote Sensing of Environment*, 113, 2651-2660, 2009.
- Jin, R., Zhang, T., Li, X., Yang, X., and Ran, Y.: Mapping surface soil freeze-thaw cycles in China based on SMMR and SSM/I brightness temperatures from 1978 to 2008, *Arctic, Antarctic, and Alpine Research*, 47, 213-229, 2015.
- Judge, J., Galantowicz, J. F., England, A. W., and Dahl, P.: Freeze/thaw classification for prairie soils using SSM/I radiobrightnesses, *Geoscience and Remote Sensing, IEEE Transactions on*, 35, 827-832, 1997.



- Kerr, Y. H., Waldteufel, P., Richaume, P., Wigneron, J.-P., Ferrazzoli, P., Mahmoodi, A., Al Bitar, A., Cabot, F., Gruhier, C., and Juglea, S. E.: The SMOS soil moisture retrieval algorithm, *Geoscience and Remote Sensing, IEEE Transactions on*, 50, 1384-1403, 2012.
- 5 Kim, Y., Kimball, J. S., McDonald, K. C., and Glassy, J.: Developing a global data record of daily landscape freeze/thaw status using satellite passive microwave remote sensing, *Geoscience and Remote Sensing, IEEE Transactions on*, 49, 949-960, 2011.
- Kim, Y., Kimball, J. S., Zhang, K., and McDonald, K. C.: Satellite detection of increasing Northern Hemisphere non-frozen seasons from 1979 to 2008: Implications for regional vegetation growth, *Remote Sensing of Environment*, 121, 472-487, 2012.
- 10 Kimball, J., McDonald, K., Keyser, A., Frohling, S., and Running, S.: Application of the NASA Scatterometer (NSCAT) for determining the daily frozen and nonfrozen landscape of Alaska, *Remote Sensing of Environment*, 75, 113-126, 2001a.
- Kimball, J. S., McDonald, K. C., Keyser, A. R., Frohling, S., and Running, S. W.: Application of the NASA Scatterometer (NSCAT) for Determining the Daily Frozen and Nonfrozen Landscape of Alaska, *Remote Sensing of Environment*, 75, 113-126, 2001b.
- 15 Li, X., Jin, R., Pan, X., Zhang, T., and Guo, J.: Changes in the near-surface soil freeze–thaw cycle on the Qinghai-Tibetan Plateau, *International Journal of Applied Earth Observation and Geoinformation*, 17, 33-42, 2012.
- Liou, Y.-A. and England, A. W.: A land-surface process/radiobrightness model with coupled heat and moisture transport for freezing soils, *Geoscience and Remote Sensing, IEEE Transactions on*, 36, 669-677, 1998.
- 20 McDonald, K. C. and Kimball, J. S.: Estimation of surface freeze–thaw states using microwave sensors, *Encyclopedia of hydrological sciences*, 2005. 2005.
- Mladenova, I. E., Jackson, T. T., Njoku, E., Bindlish, R., Cosh, M., and Chan, S.: AMSR-E-BASED SOIL MOISTURE RETRIEVAL ALGORITHMS AND TRANSFERABILITY TO AMSR2.
- Naeimi, V., Paulik, C., Bartsch, A., Wagner, W., Kidd, R., Park, S.-E., Elger, K., and Boike, J.: ASCAT Surface State Flag (SSF): Extracting information on surface freeze/thaw conditions from backscatter data using an empirical threshold-analysis algorithm, *Geoscience and Remote Sensing, IEEE Transactions on*, 50, 2566-2582, 2012.
- 25 Nelson, F. E., Anisimov, O. A., and Shiklomanov, N. I.: Subsidence risk from thawing permafrost, *Nature*, 410, 889-890, 2001.
- 30 Okuyama, A. and Imaoka, K.: Intercalibration of advanced microwave scanning radiometer-2 (AMSR2) brightness temperature, *Geoscience and Remote Sensing, IEEE Transactions on*, 53, 4568-4577, 2015.
- Parinussa, R. M., Holmes, T. R., Wanders, N., Dorigo, W. A., and de Jeu, R. A.: A Preliminary Study toward Consistent Soil Moisture from AMSR2, *Journal of Hydrometeorology*, 16, 932-947, 2015.
- Rautiainen, K., Lemmetyinen, J., Pulliainen, J., Vehvilainen, J., Drusch, M., Kontu, A., Kainulainen, J., and Seppanen, J.: L-band radiometer observations of soil processes in boreal and subarctic environments, *Geoscience and Remote Sensing, IEEE Transactions on*, 50, 1483-1497, 2012.
- 35



- Rautiainen, K., Lemmetyinen, J., Schwank, M., Kontu, A., Ménard, C. B., Mätzler, C., Drusch, M., Wiesmann, A., Ikonen, J., and Pulliainen, J.: Detection of soil freezing from L-band passive microwave observations, *Remote Sensing of Environment*, 147, 206-218, 2014.
- Schuur, E. A., Bockheim, J., Canadell, J. G., Euskirchen, E., Field, C. B., Goryachkin, S. V., Hagemann, S., 5 Kuhry, P., Lafleur, P. M., and Lee, H.: Vulnerability of permafrost carbon to climate change: implications for the global carbon cycle, *BioScience*, 58, 701-714, 2008.
- Shi, J., Zhao, T., Du, J., Ji, D., Xiong, C., Dong, X., Liu, H., Wang, Z., Jiang, L., and Du, Y.: Remote Sensing Observing Earth's water cycle from space, 2014. 2014.
- Smith, N. V., Saatchi, S. S., and Randerson, J. T.: Trends in high northern latitude soil freeze and thaw cycles 10 from 1988 to 2002, *Journal of Geophysical Research: Atmospheres*, 109, 2004.
- Zhang, L., Zhao, T., Jiang, L., and Zhao, S.: Estimate of phase transition water content in freeze–thaw process using microwave radiometer, *Geoscience and Remote Sensing, IEEE Transactions on*, 48, 4248-4255, 2010.
- Zhang, T. and Armstrong, R.: Soil freeze/thaw cycles over snow - free land detected by passive microwave remote sensing, *Geophysical Research Letters*, 28, 763-766, 2001.
- 15 Zhang, T., Armstrong, R., and Smith, J.: Investigation of the near - surface soil freeze - thaw cycle in the contiguous United States: Algorithm development and validation, *Journal of Geophysical Research: Atmospheres* (1984–2012), 108, 2003.
- Zhang, T., Barry, R. G., Knowles, K., Heginbottom, J., and Brown, J.: Statistics and characteristics of permafrost and ground - ice distribution in the Northern Hemisphere I, *Polar Geography*, 23, 132-154, 1999.
- 20 Zhao, T., Shi, J., Bindlish, R., Jackson, T., Cosh, M., Jiang, L., Zhang, Z., and Lan, H.: Parametric exponentially correlated surface emission model for L-band passive microwave soil moisture retrieval, *Physics and Chemistry of the Earth, Parts A/B/C*, 2015. 2015.
- Zhao, T., Zhang, L., Jiang, L., Zhao, S., Chai, L., and Jin, R.: A new soil freeze/thaw discriminant algorithm using AMSR - E passive microwave imagery, *Hydrological Processes*, 25, 1704-1716, 2011.
- 25 Zuerndorfer, B. and England, A. W.: Radiobrightness decision criteria for freeze/thaw boundaries, *Geoscience and Remote Sensing, IEEE Transactions on*, 30, 89-102, 1992.
- Zwieback, S., Paulik, C., and Wagner, W.: Frozen Soil Detection Based on Advanced Scatterometer Observations and Air Temperature Data as Part of Soil Moisture Retrieval, *Remote Sensing*, 7, 3206-3231, 2015.



5 **Figure 1: The comparison of AMSR-E Research Product (L1S) Tbs and that of AMSR2 Level 3 (L3) standard product at 18.7GHz and 36.5GHz displayed by color according the weight of each point. H and V are abbreviate of horizontal and vertical polarization. The color of the point is determined by the weight (density in a radius of 0.5). The darker the color is the larger the weight is.**

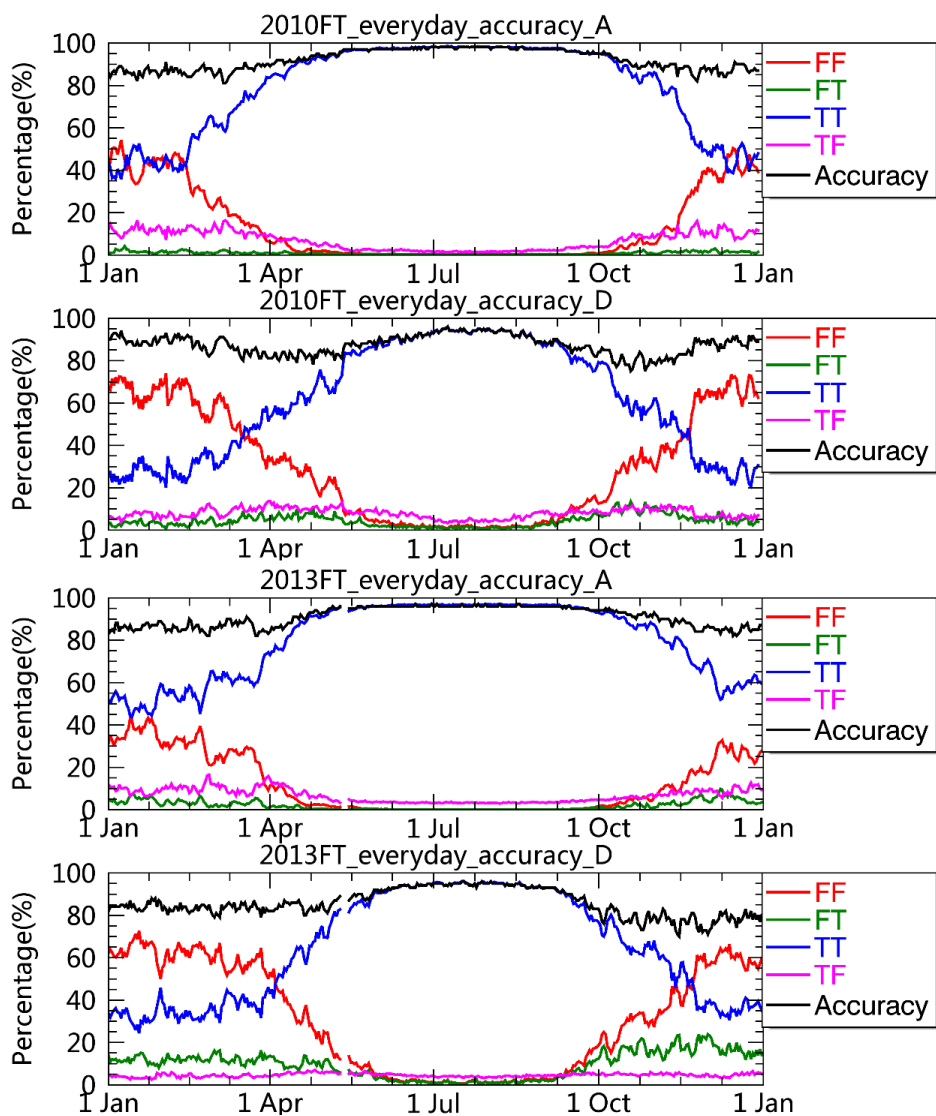


Figure 2: The black solid line is the total accuracy. The FF indicates the number percentage of that when station temperature and F/T data records are both classified as frozen and FT of that when station temperature classified as frozen while F/T data records classified as thawed. TT, TF follows the meaning like them. A means the ascending time and D means the descending time.

5

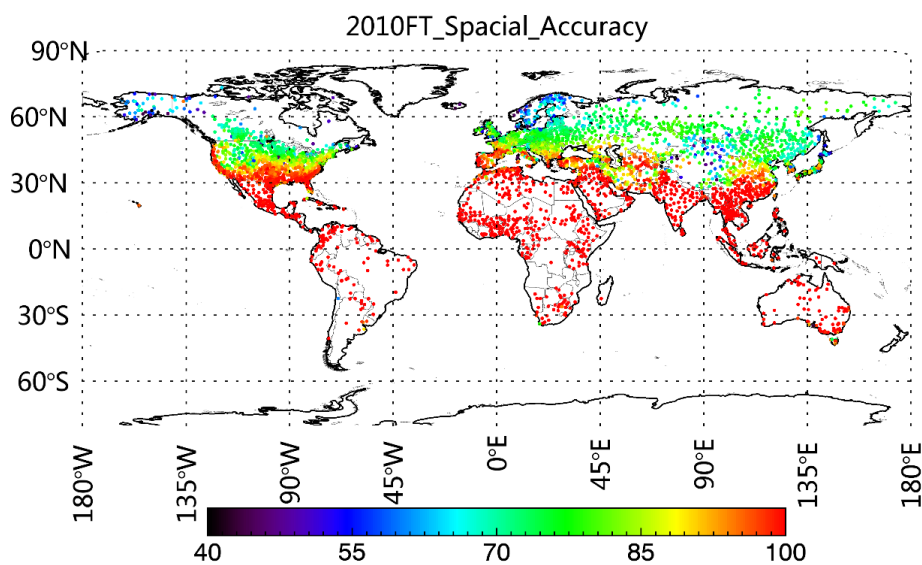


Figure 3: The distribution of stations used to estimate the accuracy on the global map. The color of the station indicates the accuracy of grid where the station located and it is the ratio of the times F/T data record results coincide with the station result divided by the total observation times of the whole year

5

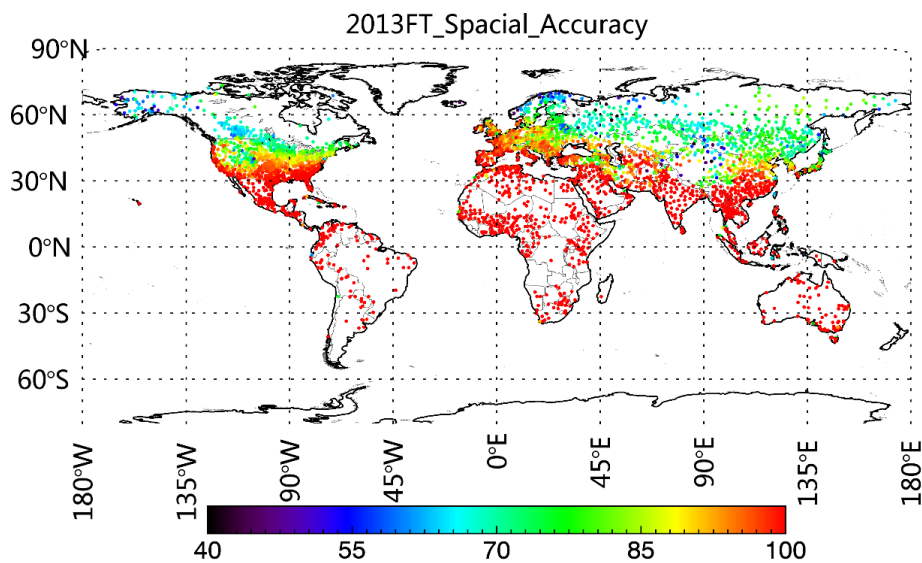


Figure 4: Same as Fig. 3 except it is the year of 2013.

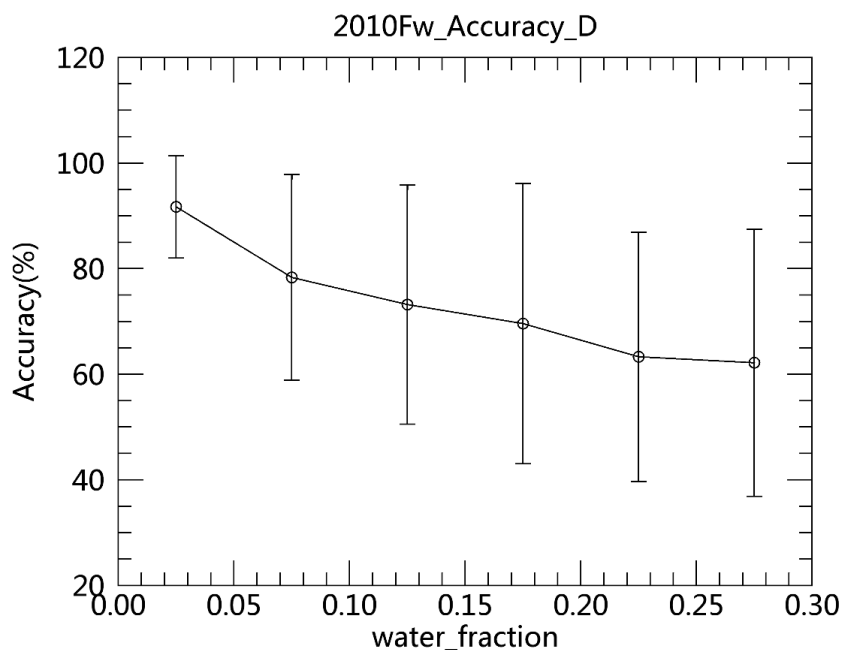
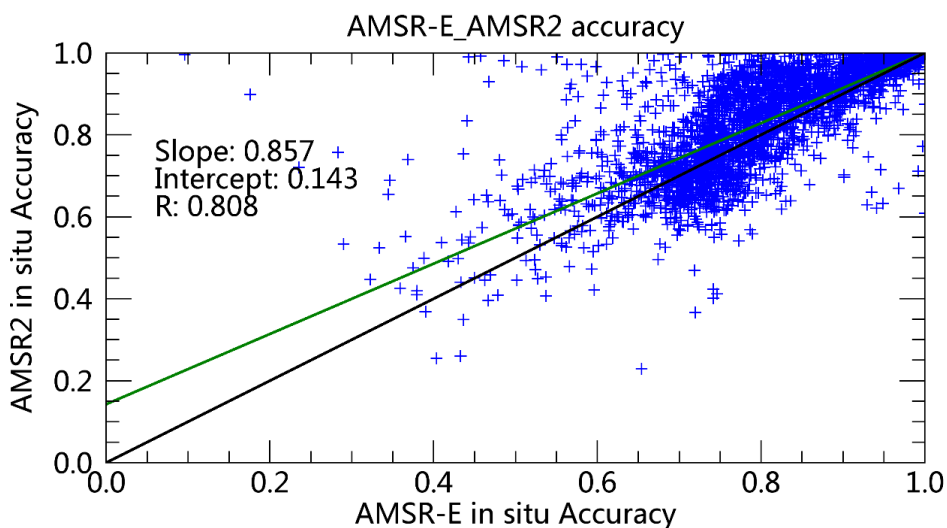


Figure5: The relationship between the accuracy and the water fraction of a pixel.



5 Figure 6: The comparison of the F/T classification accuracy at each station that are used for validation for the year of 2010 and 2013.

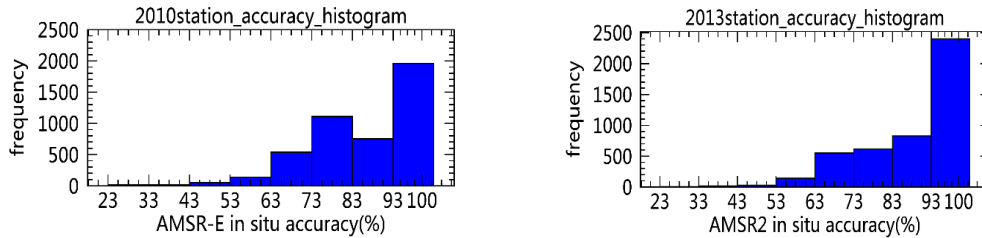
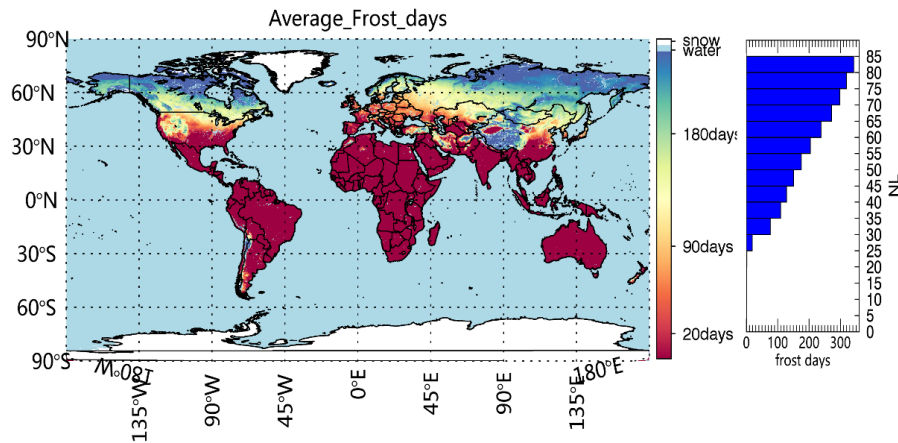


Figure 7: The histograms display the station numbers with accuracy in the zoom on the x axis.



5 Figure 8: The mean frost days of each grid calculated using ten years F/T data records (water and perennial snow areas are not included). The histogram presents the frost days variation with the latitude in the Northern Hemisphere.

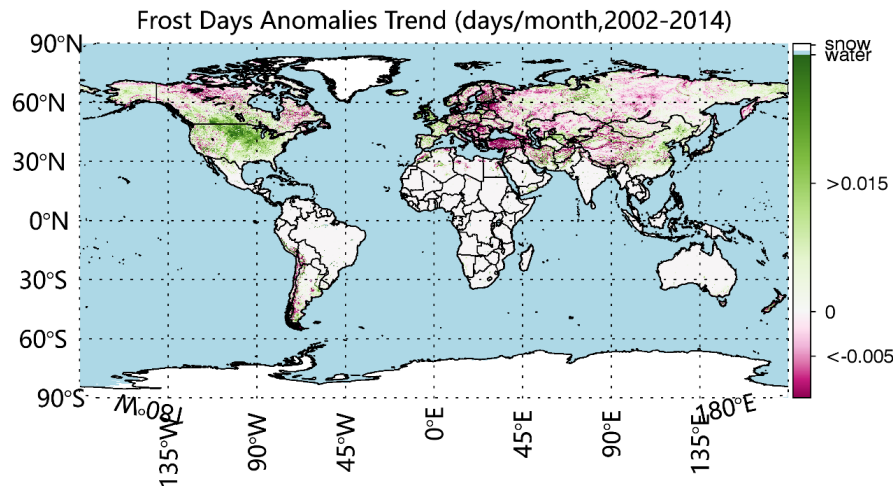


Figure 9: The linear trends (days/year) of the frost days with the least-square regressions (F-test, $p < 0.01$) and the white areas are perennial snow or the place that does not pass the F-test at a significance less than 0.01.

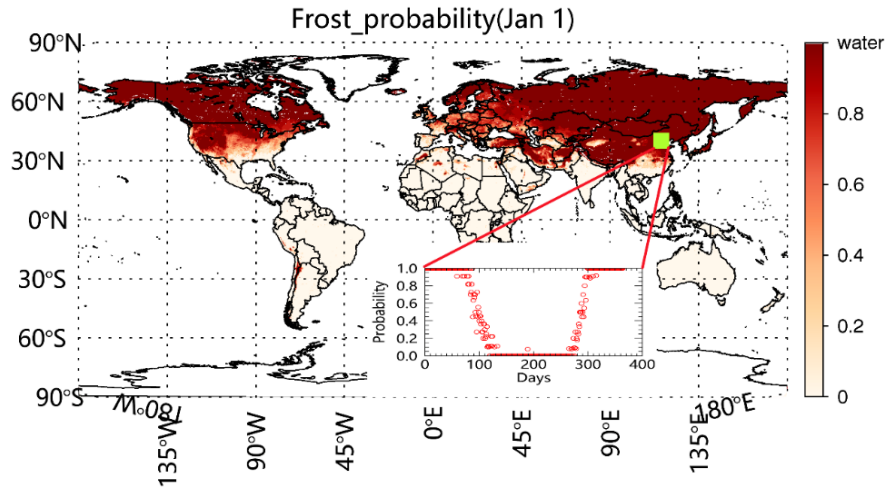
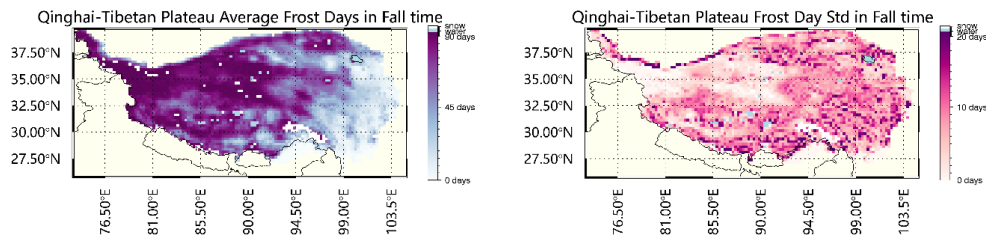


Figure 10: The frost probability on 1 Jan. and the subgraph shows the probability of a special pixel (center of the green square) on each day of a year.



5 **Figure 11a and 11b:** The average frost day and standard deviation from late fall to early winter in the Qinghai-Tibetan Plateau.

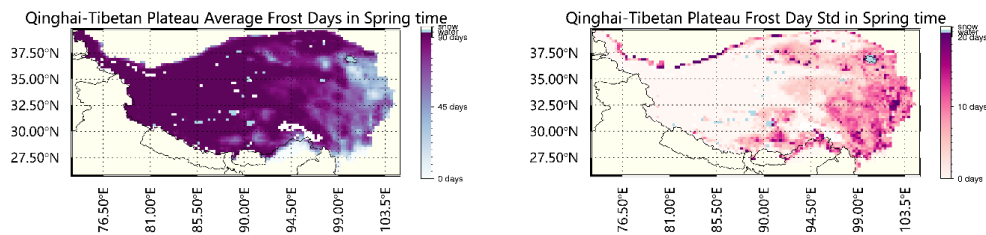


Figure 12a and 12b: The average frost day and standard deviation from late spring to early summer in the Qinghai-Tibetan Plateau.

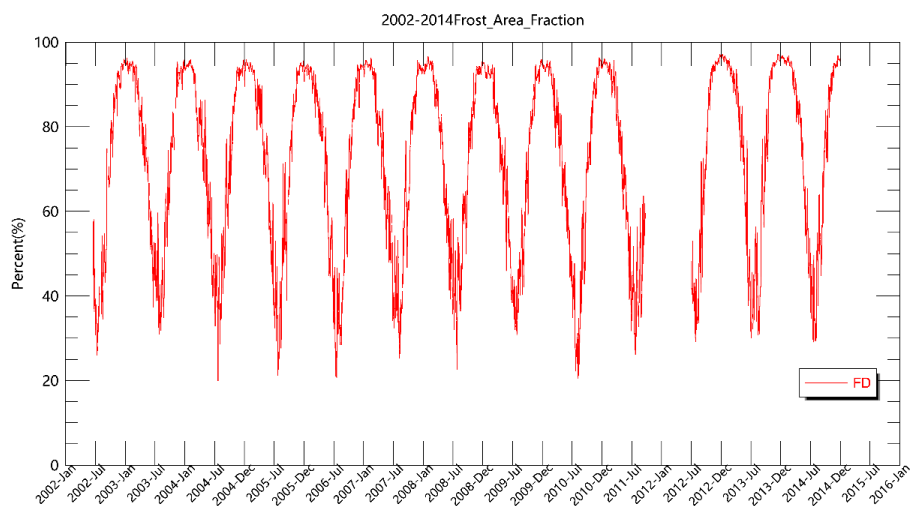
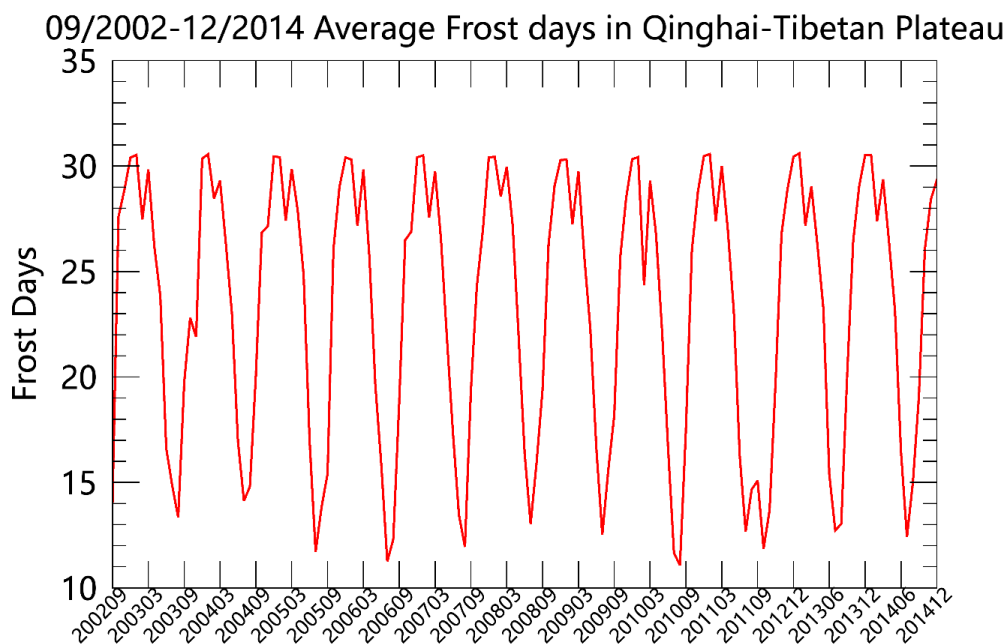


Figure 13: The fraction of area in frost status of each day (October 2011-July 2012 has no data) in the Qinghai-Tibetan Plateau.



5 Figure 14: The average frost days of each month (October 2011-July 2012 is skipped) in the Qinghai-Tibetan Plateau.

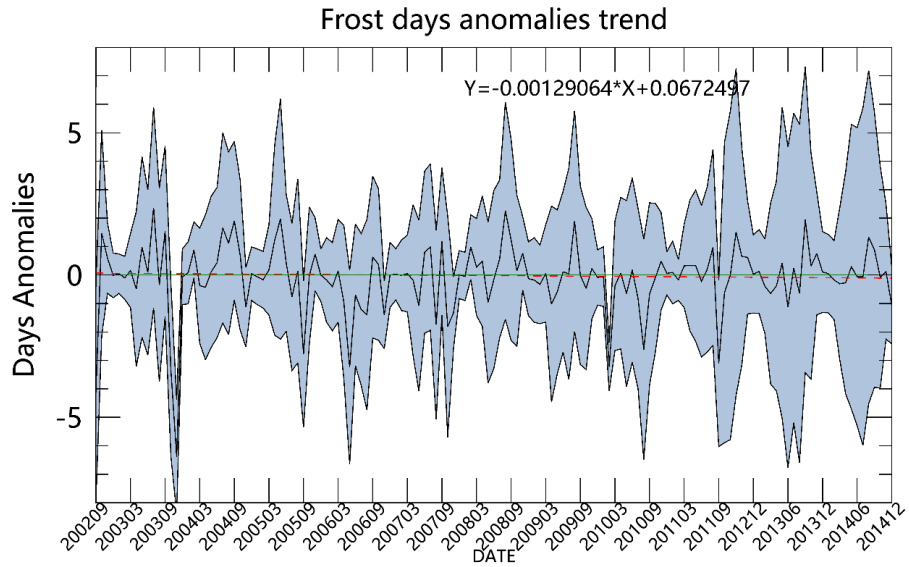
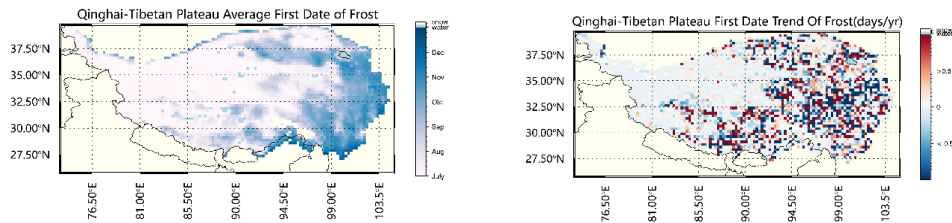


Figure 15: The frost day anomalies trend of each month (October 2011-July 2012 is skipped) in the Qinghai-Tibetan Plateau. The light blue area are the standard deviation.



5 Figure 16a and 16b: The first date of frost and its changing trend in the Qinghai-Tibetan Plateau.

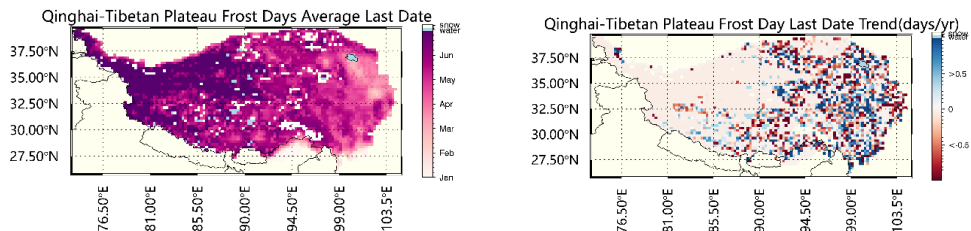


Figure 17a and 17b: The last date of frost and its changing trend in the Qinghai-Tibetan Plateau.

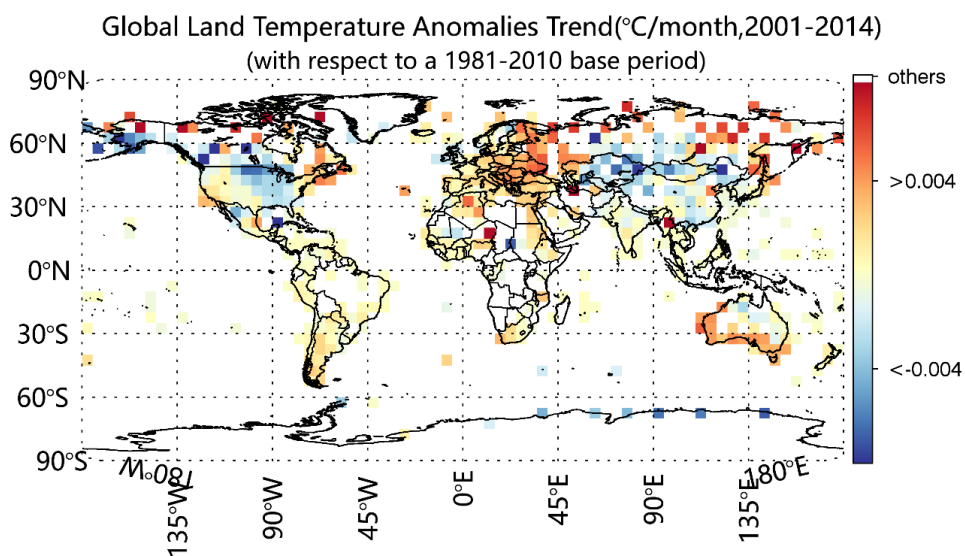


Figure 18: The linear trend of global land temperature anomalies (°C/month) of the last 14 years (2001-2014) with a confidence of 90% (F-test, $p < 0.1$). The white areas indicate no data.